INTERNATIONAL JOURNAL FOR NUMERICAL METHODS IN FLUIDS, VOL. 11, 151–168 (1990)

FREE SURFACE FLOW DURING THE FILLING OF A CYLINDER

Z. ABDULLAH AND M. SALCUDEAN

Department of Mechanical Engineering, University of British Columbia, Vancouver, BC, Canada V6T 1W5

SUMMARY

A technique is proposed to model flows with free surfaces using the control volume method. The free surface is tracked by determining the locations of the ambient pressure in the domain. Special conditions are imposed on the nodes in the vicinity of the free surface. Flow visualization experiments are carried out to determine the free surface shapes and velocity distributions during the filling of a cylindrical container with water. Computations are carried out to model the flow in the experimental test case using a mesh transformation and the free surface treatment. The proposed free surface treatment yields results of better accuracy as compared with the results using the free slip condition. The predicted locations and heights of the spout are reasonable.

KEY WORDS Free surface flows Filling of moulds Flow visualization Mathematical modelling Control Volume Method

1. INTRODUCTION

Free surface flows occur over a wide range of applications, e.g. in reservoirs, chemical reactors, moulds, ladles and tundishes. Modelling such flows poses considerable problems since the free surface profile has to be continuously tracked and the correct boundary conditions have to be applied at it. Flows during filling of moulds are even more difficult to simulate because the level of the fluid continuously rises, causing the boundaries of the computational domain to change spatially with time.

The marker and cell (MAC) and volume of fluid (VOF) methods[1–4] were developed to treat free surface flows. The Courant time step limitation[1] applies to both the MAC and VOF techniques. This restriction does not cause any additional constraints when applied to explicit codes; however, an implicit scheme would lose its advantage if the Courant limitation were required for the surface treatment. This limitation becomes increasingly restrictive with mesh refinement.

In the present work a new technique is proposed to model flows with free surfaces using the Control Volume Method.[5–8] This technique is used with a new mesh transformation to simulate the filling of a cylindrical container with water. Flow visualization experiments are also carried out to verify the predicted free surface shapes and velocity distributions.

2. EXPERIMENTAL WORK

The test section consists of a 0·121 m diameter plexiglass cylinder connected by a plastic hose with a quick-closing valve to a reservoir. The experimental conditions are isothermal. Water enters the

0271–2091/90/100151–18$09.00

Received January 1989
Revised October 1989

test section centrally from the bottom. The diameter of the inlet is 0·0121 m. Flow visualization is carried out by taking timed exposures of 0·001 m neutrally buoyant particles suspended in the fluid. A Stokes law analysis[9] has shown that the particles follow the fluid reasonably well. The smallest flow structure that can be resolved is about 0·01 m, an order of magnitude larger than the particle size.[10] A 0·01 m thick vertical light plane passing through the axis of the cylinder is produced using a slide projector and an opaque slide with a 2 mm by 20 mm slit. Photographs are taken with a Yashika FE 35 mm camera with a 50 mm lens. Black and white 125 ASA film is used and the photographs are developed to the actual size. Further details about the experimental work may be found in Reference 9.

3. MATHEMATICAL MODELLING

The flow enters centrally from the bottom of the test section in the form of a turbulent jet,[11-14] since the Reynolds number based on the orifice diameter and average fluid velocity is 2500. In the present work turbulence is simulated by the K–ε model.[15]

The conservation equations of mass, momentum and turbulence parameters are well known[13,14,16] in the primitive variable form and discretized using the Control Volume Method. A hybrid central/upwind scheme is used with the SIMPLE algorithm.[5-8] The level of the fluid rises continuously during filling. A co-ordinate transformation is employed to continuously conform the mesh to the region of the domain which mostly contains the fluid. This hybrid Eulerian–Lagrangian technique enables the mesh to 'expand' axially and conform to the rising level of the fluid. The method is similar to the approach of Watkins,[17] who employed a co-ordinate transformation to compute flows in an engine cylinder. Watkins' technique is not applicable to the problem under consideration because of the need to model the free surface. The transformation developed in this study allows only that part of the domain to expand which contains the fluid. This additional flexibility is required because the region of the domain reserved for the treatment of the free surface does not expand during filling.

3.1. Computational domain and mesh

Figure 1 shows the computational domain. The west boundary of the domain corresponds to the bottom surface of the cylinder, the north boundary corresponds to the side walls and the south boundary corresponds to the axis of symmetry. The computational domain is divided into two regions, the *fluid region* and the *free surface region.*

The *fluid region*, for which $\alpha = 1$, models that part of the cylinder which is *completely* occupied by the fluid. The control volumes in the fluid region are assumed to be completely occupied by the fluid at all times. The mesh in the fluid region expands axially (along the west–east direction) to simulate the increasing volume of the fluid during the filling of the cylinder. The 'height' of the fluid region (x_l) is determined on the basis of initial conditions, inlet flow rate and the conservation of mass principle.

The *free surface region*, for which $\alpha = 0$, models the part of the cylinder which is partly occupied by the fluid and which is expected to contain the free surface. The control volumes in the free surface region can be 'empty', 'partly full' or 'completely full' of fluid, depending on the shape of the free surface. The mesh in the free surface region does *not* expand, in order to retain the resolution required to track the free surface shape. The axial dimension of the free surface region ($x_s - x_l$) is determined at the beginning by using the conservation of energy principle on the inlet momentum of the jet.[9]

The computational domain is divided into a rectangular grid of cells (called control volumes) as shown in Figure 1. The scalar quantities (pressure and turbulence properties) are defined at the

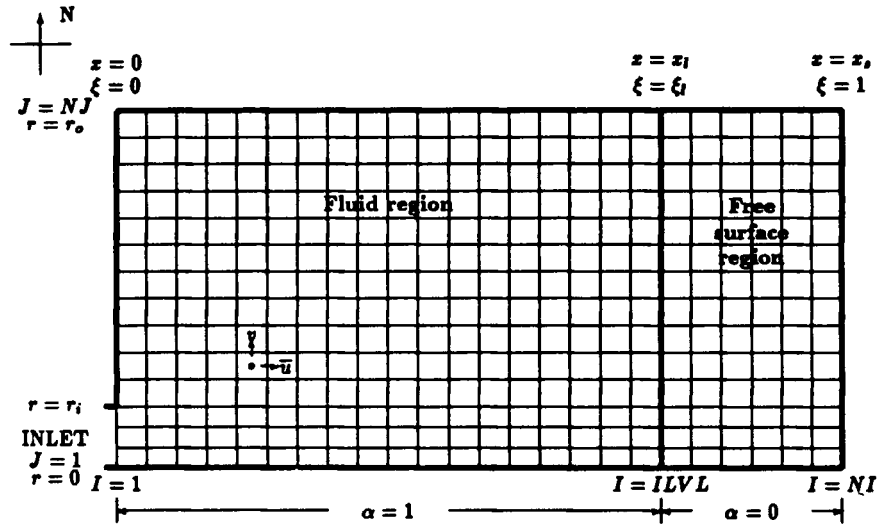

Figure 1. Computational domain

nodes which are located at the geometric cell centres. The velocity components $\bar{u}$ and v, are displaced in the x- and r-direction respectively following the staggered grid arrangement of Gosman and Ideriah.[5] Two different mesh sizes with uniform distribution were used: 20×15 and 15×13. No appreciable differences in the results were noted, and the results using the finer mesh are reported.

3.2. *Co-ordinate transformation*

The transformation maps the domain from the (x, r, t) plane to the (ξ, r, t) plane (see Figure 1). The variable ξ specifies non-dimensional axial locations and assumes constant values at the west boundary of the domain ($\xi = 0$ at $x = 0$), at the boundary between the fluid region and the free surface region ($\xi = \xi_l$ at $x = x_l$), and at the east boundary of the domain ($\xi = 1$ at $x = x_s$). The following relations hold between x and ξ:

$$\xi = \begin{cases} 0 \\ \xi_l \\ 1 \end{cases} \quad \text{for} \quad x = \begin{cases} 0, \\ x_l, \\ x_s. \end{cases} \tag{1}$$

Therefore

$$\xi = \chi_1 x + \chi_2, \tag{2}$$

where

$$\chi_1 = \frac{\alpha \xi_l}{x_l} - \frac{\alpha \xi_l - \xi_l - \alpha + 1}{x_l - x_s}, \tag{3}$$

$$\chi_2 = \xi_l - \alpha \xi_l + \frac{\alpha x_l \xi_l - \alpha x_l - x_l \xi_l + x_l}{x_l - x_s}. \tag{4}$$

The relations to transform the variables $\phi(x, r, t)$ to $\phi'(\xi, r, t)$ are given as[9]

$$\frac{\partial \phi}{\partial r}=\frac{\partial \phi'}{\partial r}, \qquad \frac{\partial \phi}{\partial x}=\chi_1 \frac{\partial \phi'}{\partial \xi}, \tag{5}$$

$$\frac{\partial \phi}{\partial t}=\frac{\partial \phi'}{\partial t}+\frac{\partial \phi'}{\partial \xi}\left[\frac{\dot{\chi}_1}{\chi_1}\xi+\chi_1 \frac{\partial}{\partial t}\left(\frac{\chi_2}{\chi_1}\right)\right]. \tag{6}$$

The grid velocity U_G is interpolated on the basis of the conditions

$$U_G=\begin{cases} 0 \\ \dot{x}_l \\ \dot{x}_s \end{cases} \quad \text{for} \quad \xi=\begin{cases} 0, \\ \xi_l, \\ 1, \end{cases} \tag{7}$$

which yields[9]

$$U_G=\chi_3 \xi+\chi_4, \tag{8}$$

where

$$\chi_3=\frac{(1-\alpha)(\dot{x}_l-\dot{x}_s)}{\xi_l-1}+\alpha\frac{\dot{x}_l}{\xi_l}, \tag{9}$$

$$\chi_4=(1-\alpha)\dot{x}_l-\xi_l\frac{(1-\alpha)(\dot{x}_l-\dot{x}_s)}{\xi_l-1}. \tag{10}$$

The velocity relative to the grid, $\bar{u}$, is related to the velocity in the inertial frame, u, by

$$\bar{u}=u-U_G. \tag{11}$$

Multiplying both sides by $\rho\phi'$, taking partial derivatives with respect to ξ, using (8) and rearranging gives[9]

$$\frac{\partial}{\partial \xi}(\rho u \phi')=\frac{\partial}{\partial \xi}(\rho \bar{u}\phi')+U_G\frac{\partial}{\partial \xi}(\rho\phi')+\rho\phi'\chi_3. \tag{12}$$

The general transport equation is written in the inertial axisymmetric cylindrical co-ordinate system as[5-8]

$$\frac{\partial}{\partial x}(\rho u\phi)+\frac{1}{r}\frac{\partial}{\partial r}(r\rho v\phi)=\frac{\partial}{\partial x}\left(\Gamma\frac{\partial \phi}{\partial x}\right)+\frac{1}{r}\frac{\partial}{\partial r}\left(r\Gamma\frac{\partial \phi}{\partial r}\right)+S_\phi-\frac{\partial(\rho\phi)}{\partial t}. \tag{13}$$

Substituting (5) and (6) and using (12) the following equation is obtained:[9]

$$\frac{\partial}{\partial t}(\rho\phi')+\left[\frac{\dot{\chi}_1}{\chi_1}\xi+\chi_1\frac{\partial}{\partial t}\left(\frac{\chi_2}{\chi_1}\right)\right]\frac{\partial}{\partial \xi}(\rho\phi')+\chi_1 U_G\frac{\partial}{\partial \xi}(\rho\phi')+\chi_1\chi_3\rho\phi'+\chi_1\frac{\partial}{\partial \xi}(\rho\bar{u}\phi')+\frac{1}{r}\frac{\partial}{\partial r}(r\rho v\phi')$$
$$=\chi_1\frac{\partial}{\partial \xi}\left(\chi_1\Gamma\frac{\partial \phi'}{\partial \xi}\right)+\frac{1}{r}\frac{\partial}{\partial r}\left(r\Gamma\frac{\partial \phi'}{\partial r}\right)+S_{\phi'}. \tag{14}$$

By substituting $\alpha=1$ and then $\alpha=0$ in (3) and (9) it can be shown that[9]

$$\chi_1\chi_3=-\frac{\dot{\chi}_1}{\chi_1}. \tag{15}$$

Substituting the above equation and the equality[9]

$$\frac{\partial}{\partial t}(\rho\phi')+(\rho\phi')\left(\frac{-\dot{\chi}_1}{\chi_1}\right)=\chi_1\frac{\partial}{\partial t}\left(\frac{\rho\phi'}{\chi_1}\right) \tag{16}$$

in (14) gives[9]

$$\left[\frac{\dot{\chi}_1}{\chi_1}\xi+\chi_1\frac{\partial}{\partial t}\left(\frac{\chi_2}{\chi_1}\right)\right]\frac{\partial}{\partial\xi}(\rho\phi')+\chi_1 U_G\frac{\partial}{\partial\xi}(\rho\phi')+\chi_1\frac{\partial}{\partial t}\left(\frac{\rho\phi'}{\chi_1}\right)-S_{\phi'}+\chi_1\frac{\partial}{\partial\xi}(\rho\bar{u}\phi')+\frac{1}{r}\frac{\partial}{\partial r}(r\rho v\phi')$$
$$=\chi_1\frac{\partial}{\partial\xi}\left(\chi_1\Gamma\frac{\partial\phi'}{\partial\xi}\right)+\frac{1}{r}\frac{\partial}{\partial r}\left(r\Gamma\frac{\partial\phi'}{\partial r}\right). \tag{17}$$

The first two terms of (17) vanish using (8) (see Appendix II) and the following equation is obtained:

$$\chi_1\frac{\partial}{\partial t}\left(\frac{\rho\phi'}{\chi_1}\right)+\chi_1\frac{\partial}{\partial\xi}(\rho\bar{u}\phi')+\frac{1}{r}\frac{\partial}{\partial r}(r\rho v\phi')=\chi_1\frac{\partial}{\partial\xi}\left(\chi_1\Gamma\frac{\partial\phi'}{\partial\xi}\right)+\frac{1}{r}\frac{\partial}{\partial r}\left(r\Gamma\frac{\partial\phi'}{\partial r}\right)+S_{\phi'}.$$

Dividing by χ_1, dropping the bar and rearranging the terms yields the general transport equation in the transformed co-ordinate system:

$$\frac{\partial}{\partial\xi}(\rho u\phi)+\frac{1}{\chi_1 r}\frac{\partial}{\partial r}(r\rho v\phi)=\frac{\partial}{\partial\xi}\left(\chi_1\Gamma\frac{\partial\phi}{\partial\xi}\right)+\frac{1}{\chi_1 r}\frac{\partial}{\partial r}\left(r\Gamma\frac{\partial\phi}{\partial r}\right)+\frac{S_\phi}{\chi_1}-\frac{\partial}{\partial t}\left(\frac{\rho\phi}{\chi_1}\right). \tag{18}$$

At this stage it is interesting to compare the general transport equation in the cylindrical co-ordinate system (equation (13)) and in the transformed cylindrical co-ordinate system (equation (18)). The differences in the two forms of the equation are (i) the axial (east–west) co-ordinate is in terms of the non-dimensional variable ξ instead of the dimensional variable x and (ii) the term χ_1 appears in equation (18). Items (i) and (ii) are closely related. Equation (3) shows that

$$\chi_1=\begin{cases}(1-\xi_l)/(x_l-x_s) & \text{for } \alpha=0,\\ \xi_l/x_l & \text{for } \alpha=1\end{cases} \tag{19}$$

is a simple linear transformation between x and ξ in the two regions of the domain shown in Figure 1. The product of the term $1/\chi_1$ with the non-dimensional co-ordinate ξ provides the actual axial co-ordinate x. When (18) is integrated over a control volume $r\mathrm{d}r\mathrm{d}\xi(1)$, the term $1/\chi_1$ combines with the volume integral to provide the actual cell volume $r\mathrm{d}r\mathrm{d}\xi(1)/\chi_1$ since $\mathrm{d}\xi$ is non-dimensional.* The value of χ_1 is determined using (19) and depends only on the grid geometry.

3.3. Variables and governing equations

The independent variables are the radial distance r and the axial distances x and ξ in the cylindrical and transformed cylindrical co-ordinate systems respectively. The dependent variables are the radial velocity v and the axial velocity $\bar{u}$. The axial velocity with respect to the inertial frame can be determined using (11) once $\bar{u}$ is known.

There are five governing differential equations to be solved. These are well known[6] and are the conservation of mass equation, two equations for the conservation of momentum (along the radial and axial directions) and two equations for the conservation of turbulence properties (turbulence kinetic energy and energy dissipation rate).

* The factor (1) in the cell volume specifies the angular dimension of the cell, which is taken as 1 radian.

Table I. Transformed source terms in the ξ, r, t system

	ϕ	Γ_ϕ	S_ϕ
Continuity	1	0	0
Radial momentum	v	μ_{eff}	$-(\partial p/\partial r)-(\mu_{\text{eff}}\, v/r^2)-\mu_{\text{eff}} v/r^2+\chi_1(\partial/\partial\xi)(\mu_{\text{eff}}\partial u/\partial r)+(\partial/r\partial r)(r\mu_{\text{eff}}\partial v/\partial r)$
Axial momentum	u	μ_{eff}	$-\chi_1(\partial p/\partial\xi)+\chi_1(\partial/\partial\xi)(\chi_1\mu_{\text{eff}}\partial u/\partial\xi)+(\partial/r\partial r)(r\mu_{\text{eff}}\chi_1\partial v/\partial\xi)$
Turbulence energy	K	$\mu_{\text{eff}}/\sigma_K$	$G-\rho\varepsilon$
Energy dissipation	ε	$\mu_{\text{eff}}/\sigma_\varepsilon$	$C_1 G_\varepsilon/K-C_2\rho\varepsilon^2/K$

Table II. Constants in the K–ε model

C_1	C_2	C_μ	σ_K	σ_ε
1·44	1·92	0·09	1·0	1·3

The equations mentioned above are written in the form of the general transport equation in the transformed co-ordinate system, equation (18), where ϕ can represent different variables. The exchange coefficients Γ_ϕ and the source terms S_ϕ are given in Table I for different ϕ.

The turbulent stresses are simulated using the effective viscosity concept. The effective viscosity is given as

$$\mu_{\text{eff}}=\mu+\mu_t, \tag{20}$$

where the turbulent viscosity is expressed as

$$\mu_t=C_\mu\rho K^2/\varepsilon. \tag{21}$$

The volumetric rate of generation of the turbulence kinetic energy is given as[18]

$$G=\mu_t\left\{2\left[\left(\frac{\partial u}{\partial x}\right)^2+\left(\frac{\partial v}{\partial r}\right)^2+\left(\frac{v}{r}\right)^2\right]+\left[\left(\frac{\partial u}{\partial r}\right)+\left(\frac{\partial v}{\partial x}\right)\right]^2-\frac{2}{3}\left[\frac{\partial u}{\partial x}+\frac{1}{r}\frac{\partial}{\partial r}(rv)\right]\right\}. \tag{22}$$

The values of the constants in the K–ε turbulence model, recommended by Launder and Spalding,[15] are given in Table II.

3.4. *Control volume equations*

The control volume equations for each variable are derived after integration of equation (18) over each volume with the appropriate assumptions about the distributions of the variables between the nodes. These procedures are quite standard and are detailed elsewhere.[5–9] The final form of the control volume equation is

$$a_P\phi_P=a_N\phi_N+a_S\phi_S+a_E\phi_E+a_W\phi_W+Sp\phi_P+Su. \tag{23}$$

In the above equation a_P, a_N, a_S, a_E and a_W represent the influence of the values of the neighbouring ϕ on the nodal ϕ-value, ϕ_P. The coefficient for the east neighbour, ϕ_E, for example, is written as[9]

$$a_E=\begin{cases}\Gamma_e A_e\chi_1/\delta\xi_e-(1/2)\rho u_e A_e & \text{for } |Pe|\le 2,\\ 0 & \text{for } Pe>2,\\ -\rho_e u_e A_e & \text{for } Pe<-2,\end{cases} \tag{24}$$

using the hybrid differencing scheme[8] to prescribe the variation of ϕ between the nodes.

Equation (23) is established for all the nodal points in the domain. The 'line-by-line' method is used with the tridiagonal matrix algorithm for the solution of the control volume equations. The SIMPLE* algorithm is used, which is well known and is described elsewhere.[8]

3.5. *Treatment of the axial momentum*

The computational grid expands along the axial (east–west) direction with a velocity specified by equation (8). The axial fluid velocity u with respect to the inertial co-ordinate system is the sum of the *Eulerian* component $\bar{u}$ computed on and with respect to the moving grid, and the *Lagrangian* component U_G, which is the grid velocity:

$$u = \bar{u} + U_G. \tag{25}$$

The momentum of the fluid due to the Lagrangian velocity component U_G has to be separately accounted for in the solution of the axial momentum equation. The control volume equation for the axial velocity with respect to the inertial frame is written as

$$a_p u_p = \sum a_i u_i + a_p^\circ u_p^\circ + Su, \tag{26}$$

where $\sum a_i u_i$ is the summation of the products of the nodal coupling coefficients a_i with the nodal velocities u_i for the north, south, east and west volumes, as shown in (23) for the general variable ϕ.

The present computations are being carried out on a moving grid and the axial velocity with respect to the grid is $\bar{u}$. Equation (26) therefore has to be written in terms of $\bar{u}$. Substituting (25) in (26) yields

$$a_p(\bar{u}_p + U_{G_p}) = \sum a_i(\bar{u}_i + U_{G_i}) + a_p^\circ(\bar{u}_p^\circ + U_{G_p}^\circ) + Su. \tag{27}$$

Rearranging the above equation to the form of (26) yields

$$a_p \bar{u}_p = \sum a_i \bar{u}_i + a_p^\circ \bar{u}_p^\circ + \overline{Su}, \tag{28}$$

where $\overline{Su}$ is written as[9]

$$\overline{Su} = Su + [a_e(U_{G_e} - U_{G_p}) + a_w(U_{G_w} - U_{G_p}) + a_p^\circ(U_{G_p}^\circ - U_{G_p})]. \tag{29}$$

The axial momentum equation therefore has additional source terms

$$Su_L = [a_e(U_{G_e} - U_{G_p}) + a_w(U_{G_w} - U_{G_p}) + a_p^\circ(U_{G_p}^\circ - U_{G_p})] \tag{30}$$

to account for the momentum generated by the velocity component due to the moving grid. The above terms can be determined explicitly using (8), since they depend on the local grid velocity and the nodal coupling coefficients.

3.6. *Free surface boundary conditions*

The boundary conditions at the free surface are that the normal and tangential stresses are zero.[19,20] Following the approach of Hirt and Shannon,[19] this condition can be written for a two-dimensional case as

$$P - 2\mu\left[n_x n_x \frac{\partial u}{\partial x} + n_x n_r\left(\frac{\partial u}{\partial r} + \frac{\partial v}{\partial x}\right) + n_r n_r \frac{\partial v}{\partial r}\right] = 0, \tag{31}$$

$$\mu\left[2n_x m_x \frac{\partial u}{\partial x} + (n_x m_r + n_r m_x)\left(\frac{\partial u}{\partial r} + \frac{\partial v}{\partial x}\right) + 2n_r m_r \frac{\partial v}{\partial r}\right] = 0, \tag{32}$$

* Semi-Implicit Method for Pressure-Linked Equations.

where n_x and n_r are the components of the normal, and m_x and m_r are the components of the tangent to the surface. Assuming that the slope of the surface is small, it can be shown that[9]

$$n_r \approx 0, \qquad n_x \approx 1, \tag{33}$$

and neglecting the viscous terms, (31) and (32) simplify to[19]

$$P \approx 0, \tag{34}$$

$$\frac{\partial v}{\partial x} \approx 0. \tag{35}$$

3.7. *Imposition of the boundary conditions near the free surface*

The computational domain is shown in Figure 1. The free surface is expected to occur in the 'free surface region', therefore it is tracked only in this region. The surface shape is approximated in a 'stepwise manner' and special boundary conditions are imposed at the cells in the vicinity of the free surface.

Each computational cell is indexed using a variable 'ISUR', the value of which determines whether the cell is treated as 'empty' or 'full', or if the free surface passes through it (see Figure 2). Table III summarizes the boundary conditions imposed on the computational cells in the vicinity

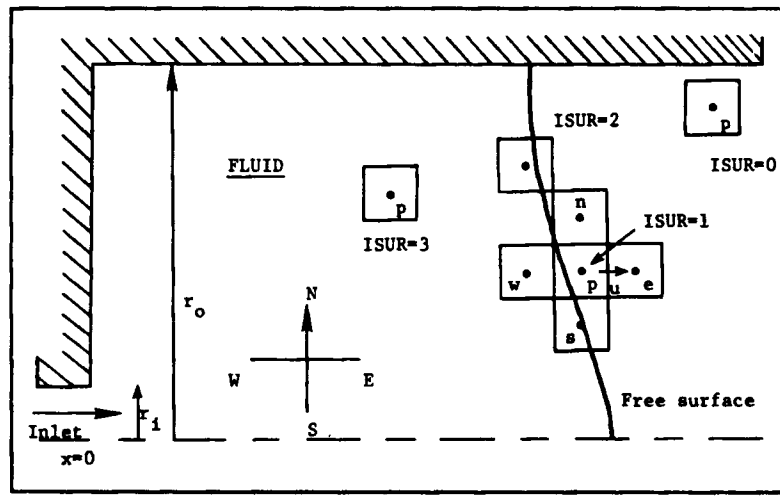

Figure 2. Cells in the free surface zone

Table III. Boundary conditions for the different cell types

$ISUR_p$	Boundary condition
0	Impose zero u, v, P, no continuity
1	Impose zero u, v, $P_s=\frac{1}{2}\rho u_s\|u_s\|$, free slip for v_{i-1}, no continuity
2	Impose $P_s=\frac{1}{2}\rho u_s\|u_s\|$, free slip for v_i, no continuity
3	No boundary conditions required

of the free surface. The conditions are applied by the manipulation of the coefficients a_i and source terms in the algebraic equation[8]

$$(a_p - Sp)\phi_p = a_n\phi_n + a_s\phi_s + a_e\phi_e + a_w\phi_w + Su, \tag{36}$$

which is obtained after the integration and discretization of (18). The nodal pressures for ISUR = 1 and ISUR = 2 are imposed assuming that the momentum of the fluid in the vertical direction is recovered in the hydrostatic pressure.

3.8. Tracking the free surface

The gravitational acceleration is accounted for in the computations, therefore the nodal pressures include the hydrostatic component. The free surface is tracked during the iterative process by searching for the 'zero'-pressure profile in the domain. At the beginning of each iteration the nodes in the free surface zone are indexed on the basis of the spatial location of the free surface. The free surface shape for the initial iteration of each time step can be obtained from either (a) an assumption of a flat surface, (b) experimental data or (c) a previous time step solution. The algorithm to track the free surface can be summarized as follows.

1. The scalar cell pair containing the free surface in each row is identified by locating the zero-pressure location.
2. The free surface location is interpolated within the cell pair and cells in the row are indexed.
3. Steps 1 and 2 are repeated for each row of cells.
4. The procedure is repeated at each iteration.

The free surface shape is updated on the basis of the nodal pressures by the steps outlined above. As convergence is approached the nodal pressures and the nodal indices become more and more 'compatible' and eventually at convergence further corrections of the nodal indices (or the free surface shape) are not required.

The conservation of mass and other properties is verified on a cell-by-cell basis and the conservation of mass is used for the computation of the pressure correction. This verification is not carried out in empty cells and in cells through which the free surface is passing because the actual location and orientation of the surface is not known. It should be emphasized that global conservation as well as conservation in the full cells *is* satisfied.

3.9. Other boundary conditions

The boundary conditions applied at the side walls and bottom surface are zero normal and tangential velocities. Therefore, for the north and west boundaries of the domain shown in Figure 2,

$$v|_{r=r_o} = 0, \qquad u|_{r=r_o} = 0, \tag{37}$$

$$v|_{x=0} = 0 \quad \text{for} \quad r_o \geqslant r > r_i, \qquad u|_{x=0} = 0 \quad \text{for } r_o \geqslant r > r_i. \tag{38}$$

A zero-gradient and zero-normal-flux condition is applied at the south boundary of the domain (Figure 2), which models the axis of symmetry:

$$v|_{r=0} = 0, \qquad \left.\frac{\partial u}{\partial r}\right|_{r=0} = 0. \tag{39}$$

The inlet condition is imposed at the west boundary for $r \leqslant r_i$. The inlet velocity varies with the level of fluid in the test section. Therefore

$$u|_{r \leqslant r_i} = u_{in}, \tag{40}$$

where u_{in} is the average inlet velocity and is an experimental parameter. The velocity profile is assumed to be uniform at the inlet.

The properties of pure water at 25°C ($\rho = 997\ \text{kg m}^{-3}$, $\mu = 8{\cdot}94 \times 10^{-4}$ kg/ms) are used.

4. DISCUSSION

Figures 3 and 4 illustrate typical results at different times during the simulation. The inlet jet penetrates from the bottom of the test section, flows towards the top and forms a spout at the free surface. The fluid then flows radially outwards and forms a vortex under the free surface. The height of the spout decreases with the increase in the level of fluid in the test section. This is to be expected since a greater portion of the momentum of the jet is redistributed in the fluid with the increase of the level. The free surface shape is predicted to be fairly flat with the exception of the spout during the initial stages of filling. Figure 5 shows the computed and experimental free surface shapes. It can be seen that in general the proposed method predicts the free surface shape quite well. The predictions at the initial time steps are less accurate because of the incorrect initial condition of a flat surface profile.

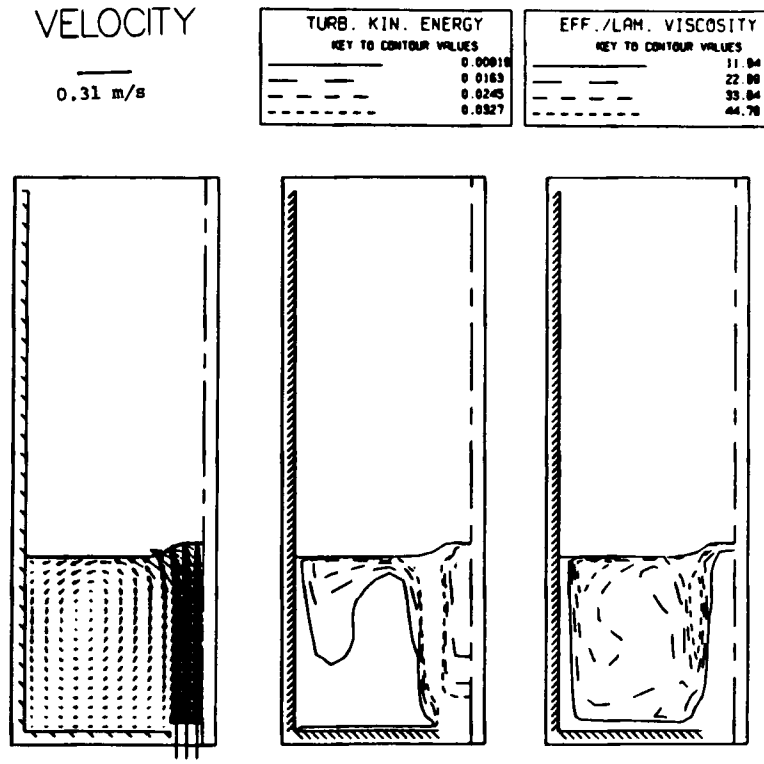

Figure 3. Velocity, turbulent energy and effective viscosity at time 4 s, level 0·059 m

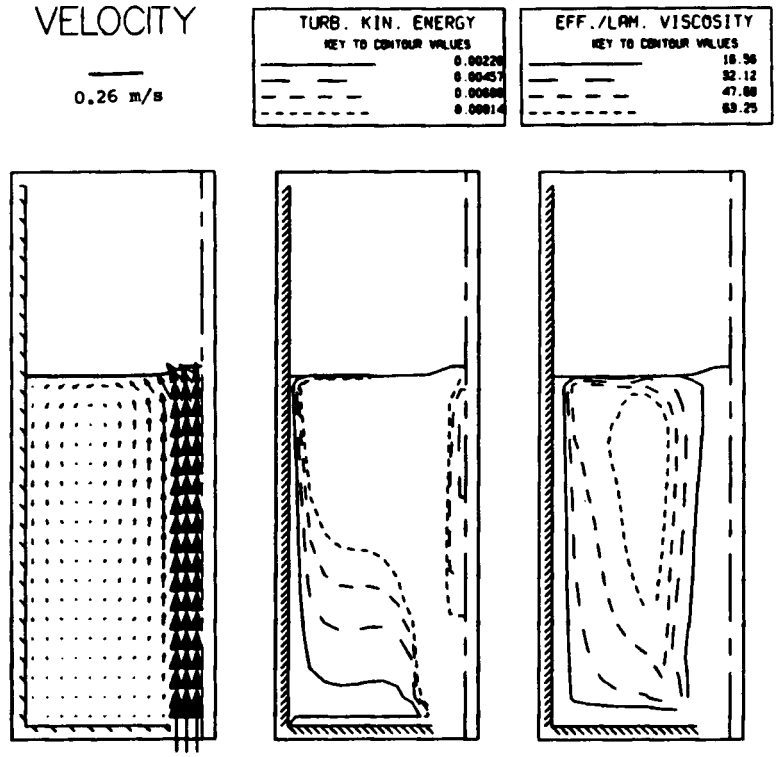

Figure 4. Velocity, turbulent energy and effective viscosity at time 11 s, level 0·119 m

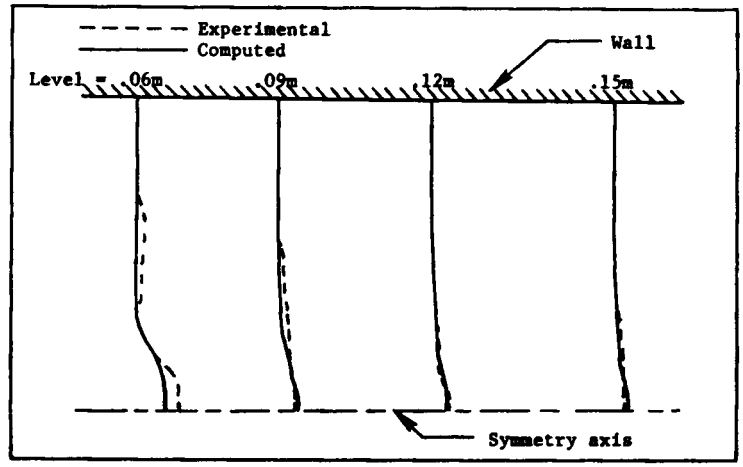

Figure 5. Experimental and computed free surface profiles

Typical contour plots of the turbulent kinetic energy and effective viscosity are also shown in Figures 3 and 4. The turbulent kinetic energy contours have been normalized to u_{in}^2 where u_{in} is the inlet velocity. The highest values of the turbulent kinetic energy are in the regions where the jet spreads into the fluid and in the vortex. The effective viscosity contours have been normalized to the laminar viscosity. The effective viscosity is high in the regions of steep velocity gradients and is between two to three orders of magnitude greater than the laminar viscosity.

Figures 6–9 show the computed velocity distributions and the photographs obtained during the filling process. The photographs contain a large number of streaklines; however, only a small fraction of these can be used to determine the velocities. Particles which enter or leave the light plane during the exposure period leave tapered streaklines, which cannot be used for the interpretation.[9] Computations were done using both the free slip condition and the free surface treatment. The plotting scales of the computed velocities are the same as those on the experimental photographs, so that an arrow and a streakline of the same length represent the same velocity magnitude. The following observations can be made.

(a) In general, for both the free surface and the free slip conditions, the computed location of the vortex appears to be closer to the surface than observed in the experiments. Figure 10 shows the computed and measured radial locations of the vortex. It may be seen that the computations with the free slip condition incorrectly predict the vortex to be further from the axis than observed experimentally. The radial position of the vortex is predicted very well when the free surface condition is used. The inlet jet impinges on a pseudo-frictionless wall when the free slip condition is used, which causes the jet to be thicker and forces the fluid radially outwards. This results in an overestimation of the radial velocities and causes the vortex to be radially further from the axis than observed experimentally or computed with the free surface condition.

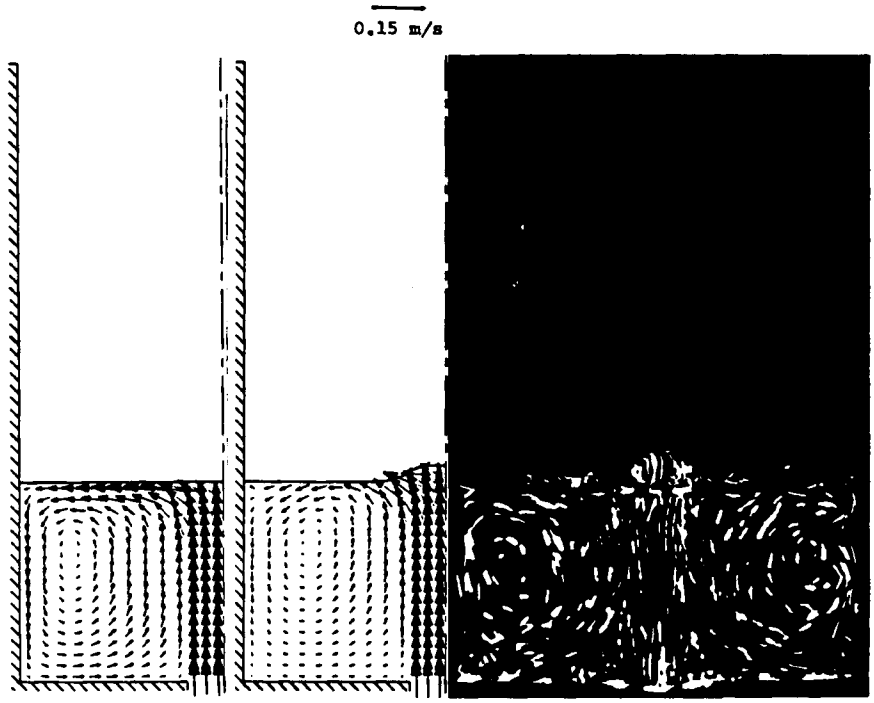

Figure 6. Experimental streakline photographs and computed velocity fields at time 4 s, level 0·059 m

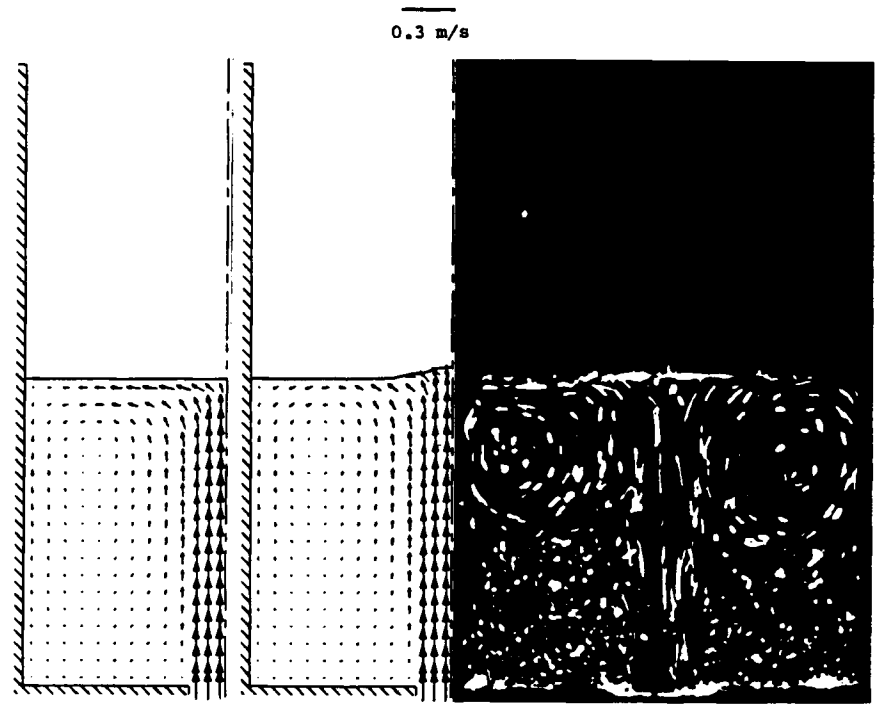

Figure 7. Experimental streakline photographs and computed velocity fields at time 7·5 s, level 0·090 m

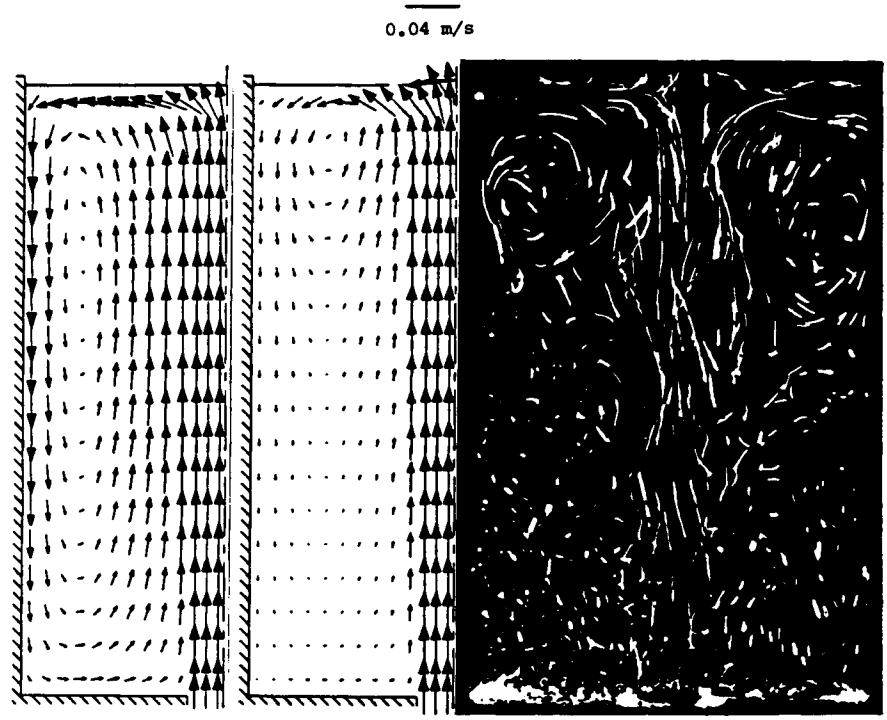

Figure 8. Experimental streakline photographs and computed velocity fields at time 15·5 s, level 0·151 m

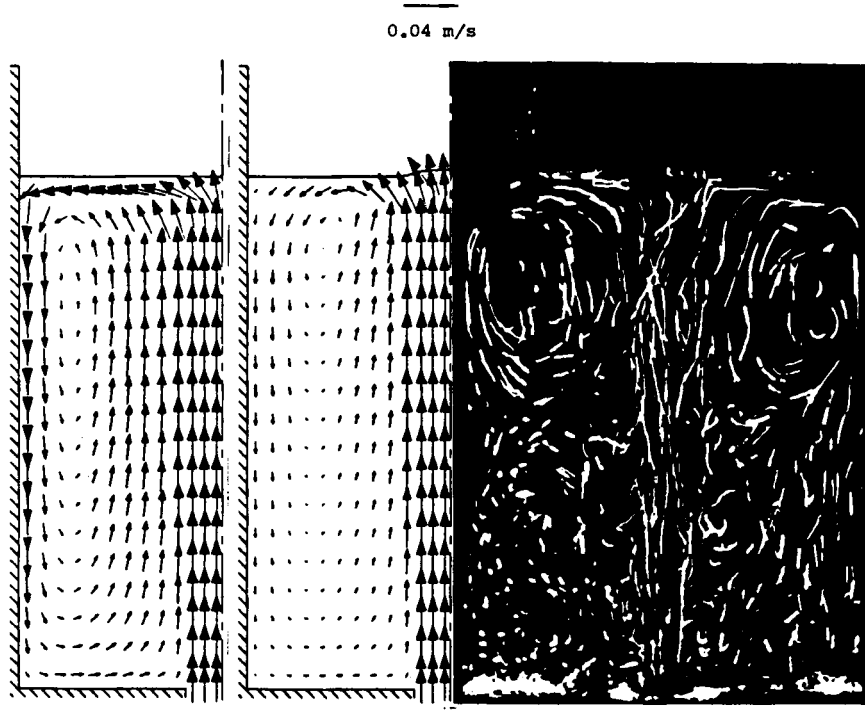

Figure 9. Experimental streakline photographs and computed velocity fields at time 20·5 s, level 0·180 m

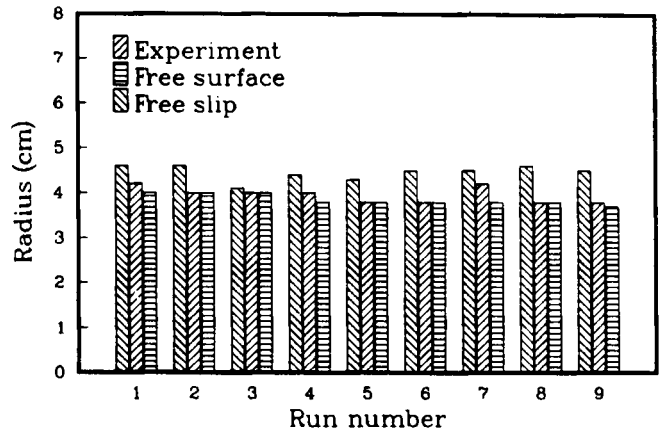

Figure 10. Computed and measured radial positions of the vortex

Figure 10 shows that the vortex radial location is predicted very accurately when the free surface condition is used.

(b) The angle of the jet appears to be too large if the free slip condition is used, since the fluid is more constrained and higher pressures occur at the surface. In the case of the free surface conditions, however, the jet angle appears to be much closer to the experimental observations, as

shown in Figures 6, 8 and 9. The jet angle cannot be determined because of the recirculatory flow pattern; however, a quantitative estimate *can* be obtained from the radial position of the vortex. Figure 10 shows that the radial position of the vortex (and therefore the jet angle) is consistently well predicted when the free surface condition is used. The larger jet angle causes the vortex to be at a greater radial distance when the free slip condition is used. The velocities predicted in the region of the spout also agree well with the experimental measurements, as evident in Figure 7.

(c) The higher radial velocities near the surface with the free slip condition also result in higher axial velocities near the walls and radial velocities at the bottom. These higher velocities are apparent in Figures 6 and 9 and would produce erroneous results in heat transfer computations. These higher velocities are a major source of discrepancy[21-23] between the computed and experimental results.

(d) In general it appears that the computed velocities are somewhat lower in magnitude as compared to the experimental results. A reason for this may be the effects of false diffusion of the momentum, since most of the flow in the vortex is inclined to the mesh. The false diffusion can somewhat suppress the overestimated velocities obtained with the free slip condition, with the result that in some cases the free slip condition appears to produce better results in some regions of the domain owing to compensation of errors.

5. CONCLUSIONS

Mathematical treatments have been developed to treat rising levels of fluids bounded by a free surface using the Control Volume approach. The methods preserve the implicit nature of the numerical technique and therefore should be more economical than the traditional Marker and Cell approach. A comparison of the computed results and experimental data indicates that the proposed method performs better than the widely used free slip assumption.

ACKNOWLEDGEMENTS

The authors wish to acknowledge the financial support of the Department of Energy, Mines and Resources, Government of Canada, and the Natural Sciences and Engineering Research Council of Canada. The computations were carried out on a Cray X-MP at the Ontario Center for Large Scale Computation.

APPENDIX I: NOMENCLATURE

a	nodal coupling coefficients
A	control volume facial area
C_1, C_2, C_μ	constants in the K–ε model
g	acceleration due to gravity
K	turbulence kinetic energy
m	tangent to the free surface
n	normal to the free surface
p	pressure
P	surface pressure
Pe	cell Peclet number defined as $\rho u \delta x/\mu$ where δx is a characteristic cell dimension
r	radial distance
S	source term
Sp	component of the linearized source term

Su	component of the linearized source term
t	time
u, v	axial and radial velocity
U_G	grid velocity
x	axial distance

Greek symbols

α	indicates fluid region ($\alpha=1$) and free surface region ($\alpha=0$)
χ	temporary variable
$\delta\xi$	normalized axial distance between a node and its neighbour
ε	energy dissipation rate
Γ	diffusion exchange coefficient
ρ	density
ϕ	general variable
σ_K	constant in the K–ε model
σ_ε	constant in the K–ε model
ξ	normalized axial distance
μ	viscosity

Subscripts

eff	effective
i	index for north, south, east, west
i	used with r for inlet radius
l	indicates the boundary between the fluid region and the free surface region
n, s, e, w	north, south, east, west
o	used with r for outer radius of cylinder
p	scalar point
r, x	radial and axial directions
s	indicates the upper limit of the cylinder height which the free surface can reach
t	turbulent
ϕ	denotes association with appropriate variable ϕ

Superscripts

$(\,)'$	indicates transformed space
$(\,)^\circ$	indicates previous time step solution
$(\bar{\ })$	relative to the grid

APPENDIX II

The objective is to demonstrate that the first two terms of (17) vanish. These terms are

$$\left[\frac{\dot{\chi}_1}{\chi_1}\xi+\chi_1\frac{\partial}{\partial t}\left(\frac{\chi_2}{\chi_1}\right)\right]\frac{\partial}{\partial\xi}(\rho\phi')+\chi_1 U_G\frac{\partial}{\partial\xi}(\rho\phi') \tag{41}$$

and can be written as

$$\chi_1\left[\frac{\dot{\chi}_1}{\chi_1^2}\xi+\frac{\partial}{\partial t}\left(\frac{\chi_2}{\chi_1}\right)\right]\frac{\partial}{\partial\xi}(\rho\phi')+\chi_1 U_G\frac{\partial}{\partial\xi}(\rho\phi').$$

Substituting $-\dot{\chi}_1/\chi_1$ from (15) in the above expression yields

$$-\chi_1\left[\chi_3\xi-\frac{\partial}{\partial t}\left(\frac{\chi_2}{\chi_1}\right)\right]\frac{\partial}{\partial\xi}(\rho\phi')+\chi_1 U_G\frac{\partial}{\partial\xi}(\rho\phi'). \tag{42}$$

Recall (8) as

$$U_G=\chi_3\xi+\chi_4. \tag{43}$$

Comparing (43) with expression (42) it may be seen that if

$$\chi_4=-\frac{\partial}{\partial t}\left(\frac{\chi_2}{\chi_1}\right), \tag{44}$$

then (42) will vanish. χ_4 is given by (10) as

$$\chi_4=(1-\alpha)\dot{x}_l-\xi_l\frac{(1-\alpha)(\dot{x}_l-\dot{x}_s)}{\xi_l-1},$$

and the time derivatives of χ_1 and χ_2, defined by (3) and (4) respectively, are

$$\frac{\partial\chi_1}{\partial t}=\frac{(\dot{x}_l-\dot{x}_s)(\alpha\xi_l-\xi_l-\alpha+1)}{(x_l-x_s)^2}-\frac{\alpha\xi_l\dot{x}_l}{x_l^2}, \tag{45}$$

$$\frac{\partial\chi_2}{\partial t}=\frac{(\dot{x}_l\alpha\xi_l-\alpha\dot{x}_l-\xi_l\dot{x}_l+\dot{x}_l)(x_l-x_s)-(\dot{x}_l-\dot{x}_s)(\alpha\xi_l x_l-\alpha x_l-\xi_l x_l+x_l)}{(x_l-x_s)^2}. \tag{46}$$

Let

$$A=-\frac{\partial}{\partial t}\left(\frac{\chi_2}{\chi_1}\right)=\frac{\dot{\chi}_1\chi_2-\dot{\chi}_2\chi_1}{\chi_1^2} \tag{47}$$

Substituting $\alpha=1$ in (3), (4), (45) and (46) yields

$$\chi_1=\frac{\xi_l}{x_l}, \qquad \dot{\chi}_1=\frac{\xi_l\dot{x}_l}{x_l^2},$$

$$\chi_2=0, \qquad \dot{\chi}_2=0.$$

Substituting χ_1, $\dot{\chi}_1$, χ_2 and $\dot{\chi}_2$ from the above in (47) gives for $\alpha=1$

$$A=0.$$

Also, from (10) it is obvious that for $\alpha=1$

$$\chi_4=0.$$

Therefore $A=\chi_4$ and (44) is valid for $\alpha=1$.

Substituting $\alpha=0$ in (3), (4), (45), (46) and (10) yields

$$\chi_1=\frac{\xi_l-1}{x_l-x_s},$$

$$\dot{\chi}_1=\frac{(1-\xi_l)(\dot{x}_l-\dot{x}_s)}{(x_l-x_s)^2},$$

$$\chi_2=\xi_l-\frac{x_l(\xi_l-1)}{x_l-x_s},$$

$$\dot{\chi}_2 = (1-\xi_l)\frac{\dot{x}_l(x_l-x_s)-x_l(\dot{x}_l-\dot{x}_s)}{(x_l-x_s)^2},$$

$$\chi_4 = \dot{x}_l - \frac{\xi_l(\dot{x}_l-\dot{x}_s)}{\xi_l-1} = \frac{\xi_l\dot{x}_s-\dot{x}_l}{\xi_l-1}. \tag{48}$$

Substitution of χ_1, χ_2, $\dot{\chi}_1$ and $\dot{\chi}_2$ in (47) and algebraic manipulation yields for $\alpha=0$

$$A = \frac{-\dot{x}_l x_l - \dot{x}_s x_s \xi_l + x_l \dot{x}_s \xi_l + \dot{x}_l x_s}{(x_l-x_s)(\xi_l-1)},$$

where the numerator can be factored as $(x_l-x_s)(\xi_l\dot{x}_s-\dot{x}_l)$, and further simplification yields

$$A = \frac{\xi_l\dot{x}_s-\dot{x}_l}{\xi_l-1}, \tag{49}$$

which is identical to (48). It has therefore been shown that for the entire domain ($\alpha=1$ and $\alpha=0$)

$$\chi_4 = -\frac{\partial}{\partial t}\left(\frac{\chi_2}{\chi_1}\right). \tag{50}$$

Hence expression (41) will vanish by virtue of (42) and (44) as discussed earlier in this appendix.

REFERENCES

1. F. H. Harlow and J. E. Welch, 'Numerical calculation of time dependant viscous incompressible flow', *Phys. Fluids*, **8**, 2182–2201 (1965).
2. C. W. Hirt and B. D. Nichols, 'Volume of fluid (VOF) method for the dynamics of free boundaries', *J. Comput. Phys.*, **39**, 201–205 (1981).
3. C. W. Hirt, B. D. Nichols and N. C. Romero, 'SOLA-A numerical solution algorithm for transient fluid flows', *Report LA-5852*, Los Alamos Scientific Laboratory, 1975.
4. B. D. Nichols, C. W. Hirt and R. D. Hotchkiss, 'SOLA-VOF: a solution algorithm for transient fluid flow with multiple free boundaries', *Report LA-8355*, Los Alamos Scientific Laboratory, 1980.
5. A. D. Gosman and F. J. K. Ideriah, 'TEACH 2E: a general computer program for two dimensional turbulent, re-circulating flows', Department of Mechanical Engineering, Imperial College, London, 1976.
6. F. J. K. Ideriah, 'Turbulent natural and forced convection in plumes and cavities', *Ph.D. Thesis*, Department of Mechanical Engineering, Imperial College, London, 1977.
7. D. G. Lilley and D. L. Rhode, 'A computer code for swirling turbulent axisymmetric re-circulating flows in practical isothermal combustor geometries', *NASA Contractor Report 3442*, 1982.
8. S. V. Patankar, *Numerical Heat Transfer and Fluid Flow*, McGraw-Hill, New York, 1982.
9. Z. Abdullah, 'Mathematical modelling of casting processes', *Ph.D. Thesis*, Department of Mechanical Engineering, University of Ottawa, 1988.
10. W. Merzkirch, *Flow Visualization*, Wiley, New York, 1974.
11. G. Birkhoff and E. H. Zarantonello, *Jets, Wakes, and Cavities*, Academic Press, New York, 1957.
12. S. I. Pai, *Fluid Dynamics of Jets*, Van Nostrand, New York, 1954.
13. H. Schlichting, *Boundary Layer Theory*, 6th edn, McGraw-Hill, New York, 1968.
14. F. M. White, *Viscous Fluid Flow*, McGraw-Hill, New York, 1974.
15. B. E. Launder and D. B. Spalding, 'The numerical computation of turbulent flows', *Comput. Methods Appl. Mech. Eng.*, **3**, 269–289 (1974).
16. D. A. Anderson, J. C. Tannehill and R. H. Pletcher, *Computational Fluid Mechanics*, McGraw-Hill, New York, 1984.
17. A. P. Watkins, *Ph.D. Thesis*, Department of Mechanical Engineering, Imperial College, University of London, 1977.
18. W. P. Jones and B. E. Launder, 'The prediction of laminarization with a two-equation model of turbulence', *Int. J. Heat Mass Transfer*, **15**, 301–314 (1972).
19. C. W. Hirt and J. P. Shannon, 'Free-surface stress conditions for incompressible-flow calculations', *J. Comput. Phys.*, **2**, 403–411 (1968).
20. L. D. Landau and E. M. Lifshitz, *Fluid Mechanics*, Pergamon, London, 1959.
21. S. Asai and J. Szekely, 'Turbulent flow and its effects in continuous casting', *Ironmaking and Steelmaking*, **3**, 205–213 (1975).
22. K. Y. M. Lai and M. Salcudean, 'Computer analysis of multidimensional turbulent, buoyancy-induced, two-phase flows in gas-agitated liquid reactors', *Comput. Fluids*, **15**, 281–295 (1987).
23. J. Szekely and R. T. Yadoya, 'The physical and mathematical modelling of the flow field in the mold region in continuous casting systems: Part II. The mathematical representation of the turbulent flow field', *Metall. Trans.*, **4**, 1379–1388 (1973).